Separation and Purification Technology 391 (2026) 137050

Contents lists available at ScienceDirect

Separation and Purification Technology

journal homepage: www.elsevier.com/locate/seppur

Experimental and dynamic modeling study of CO_2/N_2 separation on ion-exchanged binder-free LTA zeolites for post-combustion carbon capture

Mohsen Karimi [a,*], Ezzeldin Aly [b,c,d], Alírio E. Rodrigues [a], Francisco A. Da Silva Freitas [d], José A.C. Silva [b,c,**]

[a] Laboratory of Separation and Reaction Engineering (LSRE), Associate Laboratory LSRE/LCM, Department of Chemical Engineering, Faculty of Engineering, University of Porto, 4099-002 Porto, Portugal
[b] Centro de Investigação de Montanha (CIMO), Instituto Politécnico de Bragança, Campus Santa Apolónia, 5300-253 Bragança, Portugal
[c] Laboratório Associado para a Sustentabilidade e Tecnologia em Regiões de Montanha (SusTEC), Instituto Politécnico de Bragança, Campus de Santa Apolónia, 5300-253 Bragança, Portugal
[d] Aveiro Institute of Materials, CICECO, Department of Chemical Engineering, University of Aveiro, Campus Universitario de Santiago, 3810-193 Aveiro, Portugal

ARTICLE INFO

Editor Name: Yeshui Zhang

Keywords:
Zeolite
Ion-exchange
Breakthrough experiments
Response surface methodology
Net zero emissions

ABSTRACT

Ion-exchange modification of commercial binder-free zeolites offers a promising strategy to improve adsorption-based CO_2 capture from post-combustion flue gases. In this study, the CO_2/N_2 separation performance of ion-exchanged binder-free Linde-Type A (LTA) zeolites—namely 4 A, 5 A, Sr(40)A, and Sr(80)A—was systematically evaluated under post-combustion capture (PCC) conditions. Adsorption isotherms were measured over the temperature range of 306–344 K and pressures up to 350 kPa. The CO_2 uptake followed the order: 5 A > Sr(40)A > Sr(80)A > 4 A, with 5 A achieving the highest loading of 5.58 mol•kg^{-1} at 120 kPa and 306 K, compared to 4.47 mol•kg^{-1} for Sr(40)A, 4.45 mol•kg^{-1} for Sr(80)A, and 3.73 mol•kg^{-1} for 4 A. The presence of divalent cations (Ca^{2+} and Sr^{2+}) strengthened the electrostatic interactions, thereby enhancing CO_2 affinity relative to the Na-exchanged 4 A. Binary CO_2/N_2 breakthrough experiments demonstrated that Sr(80)A exhibited the highest selectivity (75 at 10 kPa and 306 K), followed by 5 A (60), 4 A (51), and Sr(40)A (47). Which the developed mathematical model accurately captured the breakthrough behavior and dynamic performance of the fixed-bed system. Finally, a Response Surface Methodology (RSM) was applied to the statistical analysis of selectivity of different studied zeolites and getting the optimum operating conditions.

1. Introduction

Addressing carbon dioxide (CO_2) emissions from industrial processes remains a critical challenge in advancing global decarbonization strategies [1,2]. Carbon Capture and Storage (CCS) has emerged as a pivotal technology in mitigating climate change and achieving net-zero emission targets [3,4]. CCS involves the capture of CO_2 generated from industrial and power generation sources, followed by its transportation to suitable storage sites and long-term sequestration in geological formations [5,6]. Within CCS, solid adsorbents play a central role due to their high efficiency and selectivity in separating CO_2 from complex emission streams [7]. Their large surface areas, tunable pore architectures, and specific molecular affinities facilitate efficient CO_2 capture while reducing the energy penalty typically associated with separation processes, thereby enhancing the cost-effectiveness of CCS systems [8,9]. Among the various solid adsorbents, porous materials such as zeolites, activated carbons, metal–organic frameworks (MOFs), and porous organic polymers have attracted considerable attention owing to their high surface areas, adjustable pore structures, and versatility in tailoring adsorption properties [10–13].

Among the zeolite families, Linde-Type A (LTA) zeolites have attracted increasing attention owing to their strong molecular sieving properties, high CO_2 adsorption capacity, and excellent selectivity [11,14,15]. Zeolite A, the first zeolite to be successfully synthesized in the laboratory [16], has remained one of the most widely used industrial adsorbents for more than five decades [1,17]. First reported by Breck et al. [16], Linde molecular sieve zeolite A consists of nearly spherical cavities with a diameter of 11.4 Å located at the center of each unit cell.

* Corresponding author.
** Corresponding author at: Centro de Investigação de Montanha (CIMO), Instituto Politécnico de Bragança, Campus Santa Apolónia, 5300-253 Bragança, Portugal.
E-mail addresses: mohsen.karimi@fe.up.pt (M. Karimi), jsilva@ipb.pt (J.A.C. Silva).

https://doi.org/10.1016/j.seppur.2026.137050
Received 18 December 2025; Received in revised form 15 January 2026; Accepted 25 January 2026
Available online 29 January 2026

These cavities are arranged in a cubic framework and interconnected with six neighboring cavities via rings of eight oxygen atoms, with each aperture providing a restricted opening of approximately 4.2 Å [18,19]. In the case of zeolite 4 A, sodium (Na^+) ions act as the exchangeable cations, with eight Na^+ ions per cavity situated near the pore openings. Their positioning effectively reduces the pore diameter to about 3.5 Å [20]. These Na^+ ions within the intracrystalline voids can be readily replaced through ion-exchange processes in aqueous solutions. Substitution of Na^+ with divalent calcium ions (Ca^{2+}) yields zeolite 5 A, which enlarges the pore openings and enables the selective adsorption of straight-chain hydrocarbons, while excluding branched-chain hydrocarbons from adsorption [16,19].

The sodium- and calcium-exchanged forms of type A zeolites, namely Linde 4 A and Linde 5 A, have been extensively investigated for gas separation applications [21–24]. Zeolite 4 A offers several advantageous properties, largely attributed to its narrower pore openings and high structural reproducibility [25,26]. By contrast, zeolite 5 A is well known for its superior CO_2 adsorption capacity, which arises from pore enlargement achieved through ion exchange, specifically the substitution of Na^+ ions with Ca^{2+} ions. This modification increases the effective pore aperture, thereby improving the accommodation and interaction of CO_2 molecules within the framework. Saha et al. [27] further demonstrated that zeolite 5 A exhibits preferential adsorption of CO_2 over CH_4 and N_2, identifying it as one of the most suitable adsorbents when compared with alternative materials such as MOF-5 and MOF-177, owing to its high equilibrium selectivity and favorable CO_2/N_2 adsorbent selection parameter.

Loughlin and Ruthven [18] demonstrated that, for Linde 5 A zeolite, both the sorption kinetics and equilibrium behavior are comparable between crystals and pellets. In contrast, Linde 4 A zeolite exhibits significantly higher diffusional resistance in pellet form relative to its crystalline counterpart. Although cation exchange only minimally alters the overall lattice dimensions, the exchangeable cations can partially obstruct the pore windows connecting adjacent cavities, thereby introducing marked variations in sorption kinetics across different cationic forms [21,22]. Despite the apparent similarity in the manufacturing processes of Linde 4 A and Linde 5 A pellets, their performance differs substantially [23,28]. This distinction is largely attributed to the well-established dependence of zeolite lattice thermal stability on the type of exchangeable cation, with the Ca^{2+}-exchanged form (5 A) demonstrating greater structural stability compared to the Na^+-exchanged form (4 A).

In certain dehydration processes, potassium-exchanged molecular sieve 3 A is preferred over 4 A due to its narrower pore openings of approximately 3 Å. This structure enables selective adsorption of small molecules such as water (dynamic diameter ~ 2.8 Å), while excluding larger molecules such as alcohols and heavier hydrocarbons [29]. Coughlan and Shaw [30] systematically investigated the sorption properties of Type A zeolites exchanged with various metal ions, including Na^+, K^+, Li^+, Ag^+, Ca^{2+}, Sr^{2+}, Co^{2+}, Ni^{2+}, Zn^{2+}, and Cd^{2+}. At 333.15 K and ~ 25 kPa, the CO_2 uptake sequence was reported as: CaA > SrA > NaA > LiA > > NiA > CdA = ZnA > CoA. Strontium-exchanged zeolite A (SrA) ranked second in CO_2 uptake, positioned between CaA (5 A) and NaA (4 A), with the performance strongly influenced by the location of exchangeable cations. Cations situated near six- and eight-membered rings extending into the supercage generate high-energy adsorption sites for quadrupolar CO_2 due to the strong electric fields and field gradients [30]. X-ray diffraction studies further confirmed that Sr^{2+} ions predominantly occupy the centers of six-membered rings, with ~80% extending into the supercage and the remaining ~20% located in the sodalite units [31]. Also, some interesting detailed molecular-level analyses of CO_2–cation interactions on LTA zeolites can be found in [17,32–36]. These findings highlight the strong potential of SrA for gas adsorption applications. However, literature on Sr-exchanged A-type zeolites remains limited, motivating the present study, which systematically investigates binder-free 4 A, 5 A, and SrA zeolites for CO_2 capture.

1.1. Research objectives

The objective of this study is to rigorously determine how cation exchange in binder-free Linde-Type A zeolites governs their suitability for post-combustion CO_2 capture, by coupling systematic experiments with predictive modeling. Specifically, the work compares Na- (4 A), Ca- (5 A), and Sr-exchanged (Sr(40)A, Sr(80)A) LTA beads through single- and binary fixed-bed breakthrough tests across 306–344 K and relevant partial pressures, extracting multicomponent equilibria with a dual-site Langmuir framework, quantifying adsorption energetics via isosteric heats, and validating bed-scale transport with Aspen Adsorption. Afterwards, a Response Surface Methodology was developed for statistical analysis of selectivity of different studied zeolites for CO_2/N_2 separation. Using selectivity and pressure-swing working capacity as process-relevant performance metrics, the study identifies how cation identity and exchange degree modulate CO_2 affinity, N_2 co-adsorption, and mass-transfer/dispersion effects, and benchmarks LTA variants against literature adsorbents. The overarching aim is to deliver experimentally anchored parameters and a vetted dynamic model that together nominate the most promising LTA formulation(s) and operating window for integration into VPSA-type PCC processes.

2. Materials and methods

2.1. Adsorbent and adsorbate

All zeolite materials investigated in this study were supplied in binder-free bead form by Chemiewerk Bas Köstritz GmbH (Germany), ensuring industrially relevant morphology and mechanical integrity for fixed-bed applications. Commercial binder-free LTA-type zeolites in the Na^+ (4 A, Köstrolith® 4ABFK) and Ca^{2+} (5 A, Köstrolith® 5ABFK) forms were employed as received. The materials were supplied as spherical beads with particle diameters in the range of 1.6–2.5 mm. All LTA zeolites examined in this work possess a Si/Al ratio of 1. Strontium-exchanged LTA zeolites were prepared via controlled aqueous ion-exchange starting from the binder-free 4 A material (Köstrolith® 4ABFK) by Chemiewerk Bas Köstritz GmbH (Germany). In this process, the parent Na–LTA beads were contacted with an aqueous strontium salt solution (typically $SrCl_2$) under controlled temperature and continuous agitation for a defined exchange period. The degree of Sr^{2+} exchange was adjusted by varying the number of ion-exchange cycles and exchange conditions (solution concentration, contact time, and liquid-to-solid ratio), with intermediate washing steps using deionized water to remove residual electrolyte. After completion of the exchange process, the beads were thoroughly washed, dried, and thermally activated prior to adsorption measurements. The resulting materials exhibited nominal Sr^{2+} exchange degrees of 40% and 80%, herein referred to as Sr(40)A and Sr(80)A, respectively. The exchange degrees were determined and certified by the supplier based on elemental composition analysis.

All zeolite samples were investigated as received from the supplier and were activated under appropriate conditions prior to adsorption measurements. The use of binder-free commercial beads ensures that the reported equilibrium, kinetic, and dynamic data are directly relevant to industrial fixed-bed adsorption processes. Also, the adsorptive and carrier gases were supplied by Air Liquide with the following certified purities: helium (He), ALPHAGAZ 2 (99.9998% purity); carbon dioxide (CO_2), N48 (99.998% purity); and nitrogen (N_2), N50 (99.999% purity).

2.2. Characterization

The detailed textural characterization of the binder-free LTA zeolite beads was carried out through nitrogen adsorption–desorption analysis at cryogenic temperature (77 K) using an accelerated surface area and porosimetry analyzer (ASAP® 2420, Micromeritics) (as reported in

Table S1, Supporting Information). The adsorption measurements were performed over the relative pressure range corresponding to absolute pressures up to 101.3 kPa, allowing for accurate determination of the specific surface area and pore volume distribution. Before analysis, all samples underwent thermal activation to eliminate moisture and any residual adsorbates. Degassing was conducted under high-vacuum conditions ($\leq 10^{-7}$ mbar) at 573 K for a duration of 12 h, ensuring complete regeneration of the microporous framework and full accessibility of adsorption sites. To complement the gas sorption data and to gain further insight into the pore structure, mercury intrusion porosimetry (MIP) was performed using a Micromeritics AutoPore IV 9500 porosimeter. The measurements were carried out using a non-wetting mercury phase with an applied contact angle of 130°, over a pressure range extending from 0.003 MPa to 207 MPa. This approach provided information on the interparticle voids and macropore connectivity within the spherical beads. The MIP samples were subjected to the same activation treatment as used for the N_2 adsorption tests to maintain consistency in pore accessibility. The surface morphology and structural homogeneity of the LTA zeolite beads were further examined by scanning electron microscopy (SEM) using a JEOL JSM-6490 microscope equipped with a secondary-electron detector. The instrument, capable of achieving a spatial resolution of approximately 3.0 nm, enabled detailed visualization of the external surface texture, grain boundaries, and particle uniformity. These combined characterization techniques ensured a comprehensive assessment of the structural and morphological features governing the adsorption behavior of the binder-free LTA zeolites.

2.3. Experimental procedure

A single- and multicomponent breakthrough apparatus was employed to investigate the fixed-bed adsorption dynamics of CO_2 and N_2, as well as to determine adsorption equilibrium data. The detailed configuration of the setup and the corresponding experimental procedures have been reported previously [37]. However, the detailed specifications and geometric characteristics of the adsorption bed are provided in Table S2 (Supporting Information).

2.4. Adsorption equilibrium model

Single- and multicomponent adsorption behaviors of the LTA zeolite samples were evaluated through dynamic fixed-bed experiments, and the resulting equilibrium data were analyzed using the dual-site Langmuir (DSL) isotherm model [38]. This model was selected because it effectively captures the intrinsic heterogeneity of the zeolitic framework, in which two classes of adsorption sites coexist-typically representing sites of high and low energetic affinity toward the adsorbate molecules [39]. By distinguishing between these surface domains, the DSL model provides a more realistic description of the adsorption process compared to the conventional single-site Langmuir formulation, particularly for materials exhibiting strong electrostatic fields or cationic heterogeneity such as LTA zeolites. For gas mixtures, the extended form of the DSL approach was employed to account for competitive adsorption phenomena, enabling accurate prediction of multicomponent equilibria based on single-component parameters [38,40]. Moreover, the temperature dependence of the affinity constant was described through a van't Hoff-type relationship, which links the adsorption strength to the enthalpic interaction between adsorbate and framework [41]. This thermodynamic treatment allows the model to reflect variations in binding energy with temperature, offering insight into the energetic diversity and adsorption selectivity of the zeolite. Overall, the DSL-based analysis provided a consistent and physically meaningful interpretation of the adsorption data, bridging experimental observations with the underlying microscopic characteristics of the LTA structure [39]. The detailed information of this model and related parameters are described in Supporting Information.

2.5. Isosteric heat of adsorption

The isosteric heat of adsorption (q_{st}) was evaluated to quantify the energetic interactions between the adsorbate molecules and the LTA zeolite surface [38,42]. This parameter reflects the strength of the adsorbate–adsorbent bonding and provides direct insight into the heterogeneity of adsorption sites. It was determined using the Clausius–Clapeyron thermodynamic relationship, which describes how the equilibrium pressure varies with temperature at constant surface coverage. In practice, the value of q_{st} can be obtained from the slope of the linear correlation between the logarithm of equilibrium pressure and the reciprocal of absolute temperature at a fixed loading [39,43]. Alternatively, a numerical approach based on differentiation of the dual-site Langmuir (DSL) model was employed, which allows prediction of the local adsorption enthalpy associated with each class of adsorption sites. This method captures the contribution of both high- and low-energy sites, reflecting the structural and energetic heterogeneity inherent to the LTA framework. The positive magnitude of q_{st} corresponds to the exothermic nature of the adsorption process, with higher values indicating stronger interactions between CO_2 molecules and the zeolitic surface. Consequently, analysis of the isosteric heat provides a valuable tool for correlating adsorption thermodynamics with the distribution of active sites and the overall selectivity of the material [39]. The detailed information and considered parameters are described in Supporting Information.

2.6. Adsorption performance metrics

The adsorption performance of the LTA zeolites was evaluated in terms of two essential thermodynamic indicators: selectivity and working capacity. The selectivity (α) represents the ability of an adsorbent to preferentially capture one gas component in the presence of others, serving as a direct measure of separation efficiency in multicomponent systems [40,44]. It reflects the ratio of relative uptakes normalized by the corresponding partial pressures of the components, thereby indicating how strongly the adsorbent discriminates between competing species under identical thermodynamic conditions. In this study, the selectivity of component i over component j was determined using equilibrium loadings derived from the dual-site Langmuir (DSL) model, which enables accurate prediction of competitive adsorption behavior within heterogeneous zeolitic frameworks. Complementarily, the working capacity was employed as a practical performance metric to assess the cyclic adsorption potential of the material. It quantifies the difference between the amount of gas adsorbed during the capture step and the amount released during regeneration, thus reflecting the effective quantity of gas that can be processed per cycle under given operating conditions [40]. Both temperature and pressure were incorporated into the calculation of working capacity to simulate realistic process scenarios. Collectively, these two parameters - selectivity and working capacity-provide an integrated assessment of the thermodynamic and operational performance of the LTA zeolites, offering critical insights into their suitability for gas separation and CO_2 capture applications. More details accompanied with calculated parameters are available in Supporting Information.

2.7. Breakthrough mathematical modeling

Numerical simulations of the fixed-bed adsorption breakthrough experiments were carried out using the Aspen Adsorption v.10 software package, following a validated modeling framework previously established in the literature [45,46]. The model incorporated a comprehensive set of governing equations describing mass, energy, and momentum balances within the adsorption column, as summarized in Table S3 (Supporting Information), while the empirical and semi-empirical correlations employed for the estimation of transport parameters are provided in Table S4. These correlations facilitated the determination of

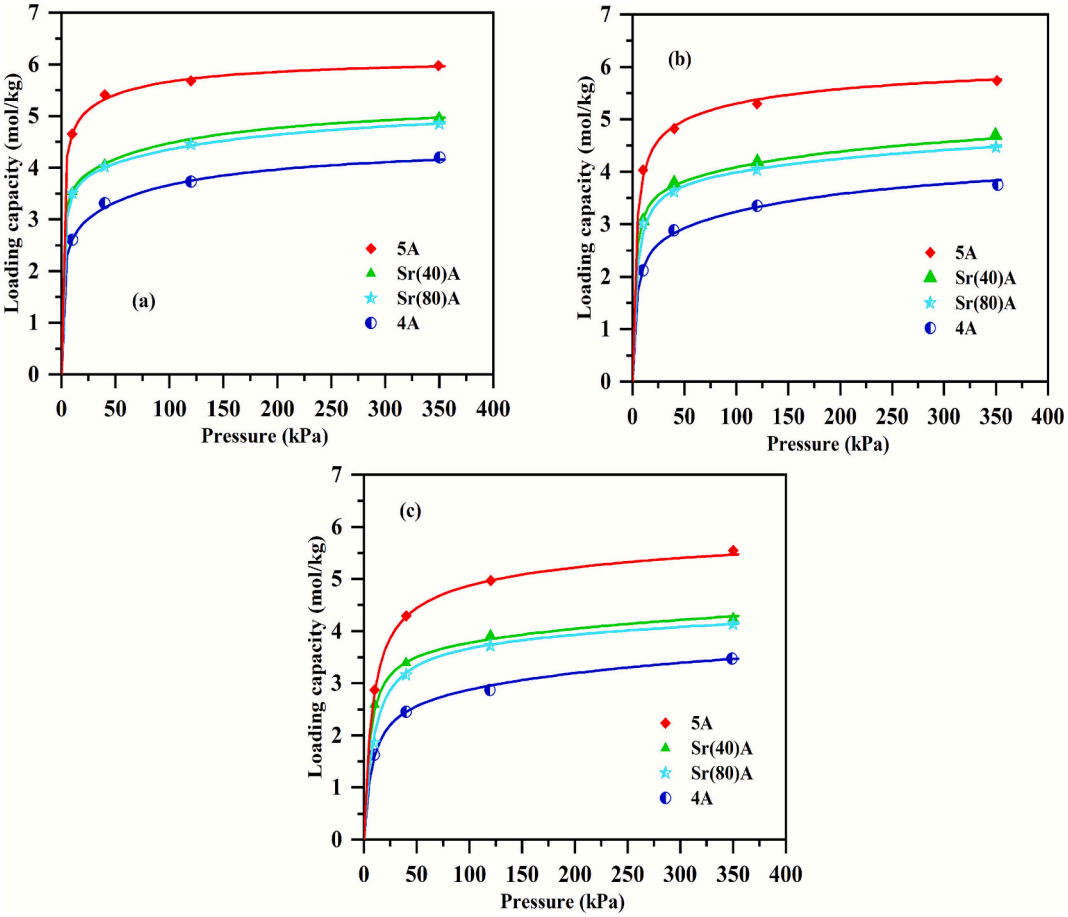

Fig. 1. Comparison of CO_2 adsorption isotherms at **(a)** 306, **(b)** 326, and **(c)** 344 K between binder-free 4 A, 5 A, Sr(40)A, Sr(80)A zeolite. Experimental = symbols; DSL isotherm = lines.

critical kinetic descriptors, such as the overall mass transfer coefficient and the axial dispersion term, which collectively define the dynamic response of the adsorption front within the packed bed. Accurate evaluation of these parameters was essential for reproducing the characteristic shape and progression of the breakthrough curves, particularly in capturing the broadening of the mass transfer zone under different operating conditions. The model further accounted for non-isothermal effects, interparticle diffusion resistance, and gas-phase dispersion to ensure consistency with the experimental behavior. The relevant physical and geometrical properties of the packed bed, as well as those of the adsorbent particles employed in the simulations, are detailed in Supporting Information. This comprehensive modeling approach provided a reliable predictive tool for interpreting the experimental data and elucidating the underlying mass transfer mechanisms governing the adsorption process.

2.8. Statistical analysis by RSM

A rigorous statistical analysis of the adsorption equilibrium data was performed using Response Surface Methodology (RSM), which combines mathematical modeling with statistical inference to explore variable interactions, identify governing trends, and determine optimal operating conditions [24,47]. RSM is particularly well suited to adsorption systems, as it allows key performance metrics—such as CO_2/N_2 selectivity—to be expressed explicitly as continuous functions of operating parameters, including temperature and pressure. Within this framework, the process variables are treated as independent factors, while the adsorption responses are represented as continuous response surfaces [48]. The statistical significance of individual factors and their interactions was subsequently assessed through analysis of variance (ANOVA).

In this study, statistical modeling was carried out using the Historical Data module of Design-Expert® software (v8.0). Temperature and pressure were selected as the independent variables, whereas adsorption selectivity was defined as the response of interest. The relationship between factors and response was described using a second order (quadratic) polynomial model, given by [49]:

$$y = \beta_0 + \beta_1 x_1 + \beta_2 x_2 + \beta_{12} x_1 x_2 + \beta_{11} {x_1}^2 + \beta_{22} {x_2}^2 + \varepsilon \quad (1)$$

In this formulation, y represents the predicted response, while x_1 and x_2 denote the coded independent variables, each evaluated at three levels (−1, 0, and + 1) [50,51]. The coefficients β_1 and β_2 correspond to the linear effects, β_{12}accounts for the interaction between the variables, and β_{11} and β_{22}describe the quadratic contributions. The terms β_0 and ε represent the intercept and the residual error, respectively [47]. Model coefficients were determined using multiple regression analysis based on the least-squares approach, and their statistical relevance was verified through p-value analysis, ensuring an insignificant lack-of-fit [50].

The reliability and predictive accuracy of the developed response surfaces were evaluated using the standard deviation (Eq. (2)), along with the coefficients of determination (R^2 and adjusted R^2, Eqs. (3) and (4)):

$$Std.Dev. = \sqrt{\frac{\sum_{i=1}^{n} (y_i - \hat{y}_i)^2}{n - P}} \quad (2)$$

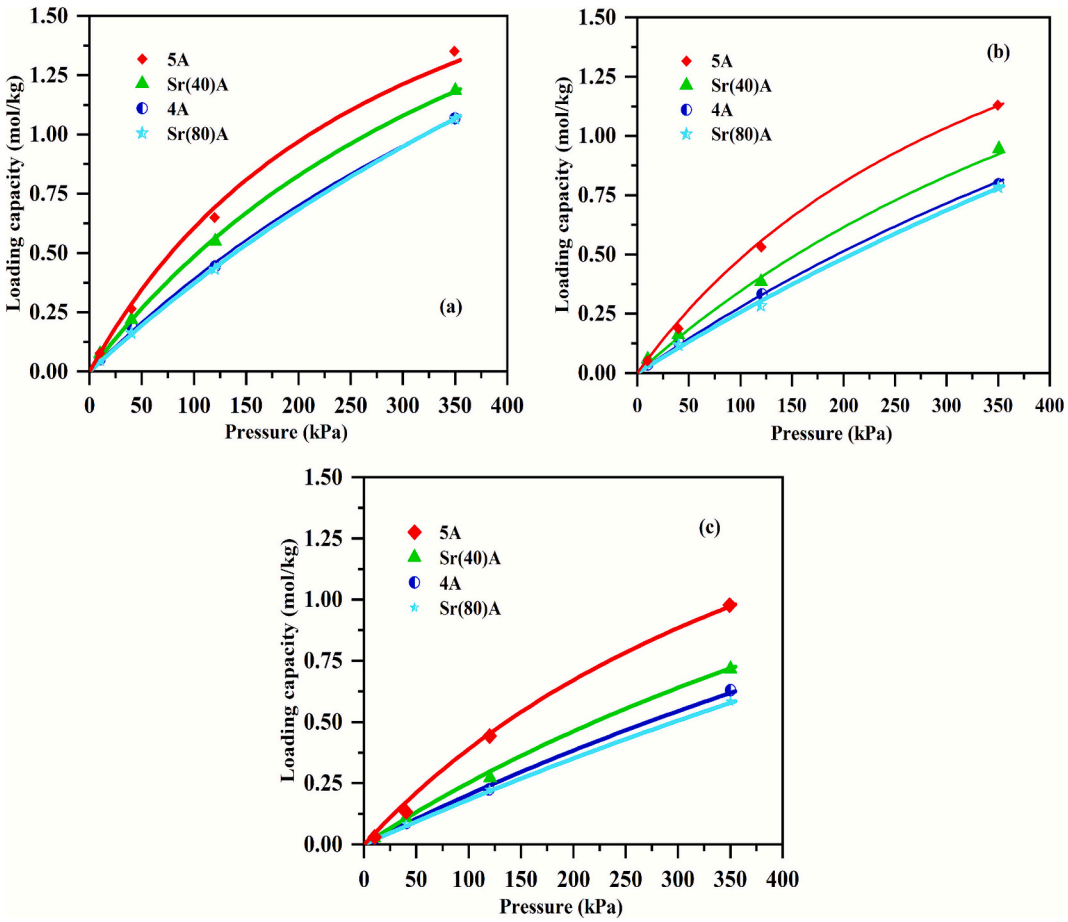

Fig. 2. Comparison of N_2 adsorption isotherms at **(a)** 306, **(b)** 326, and **(c)** 344 K between binder-free 4 A, 5 A, Sr(40)A, Sr(80)A zeolite. Experimental = symbols; DSL isotherm = lines.

$$R^2 = 1 - \frac{\sum_{i=1}^{n}(y_i - \hat{y}_i)^2}{\sum_{i=1}^{n}(y_i - \bar{y})^2} \tag{3}$$

$$AdjR^2 = 1 - \frac{(1-R^2).(n-1)}{(n-P-1)} \tag{4}$$

where n denotes the number of experimental observations, p the number of model predictors, and, $\hat{y}_i$ and y_i are the estimated data and experimental results, respectively [47]. Collectively, these statistical indicators confirm that the proposed quadratic models provide a robust and quantitative representation of adsorption selectivity behavior as a function of temperature and pressure.

3. Results and discussion

3.1. Adsorbent properties and characterization

The textural properties of the adsorbents were characterized by N_2 gas sorption (Fig. S1, Supporting Information), mercury (Hg) intrusion porosimetry (Fig. S1b), and scanning electron microscopy (SEM) (Figs. S1c–f). The corresponding data for the binder-free 5 A zeolite are summarized in Table S1. The N_2 adsorption isotherm exhibited a steep uptake at low relative pressures ($p/p_o = 10^{-4}$–10^{-2}), reflecting strong gas–solid interactions within narrow micropores and subsequent pore filling. The adsorbed volume increased from ≈140 $cm^3 \bullet g^{-1}$ to ≈180 $cm^3 \bullet g^{-1}$, reaching a plateau following micropore saturation. At higher relative pressures ($p/p_o \approx 0.9$), a slight additional uptake was observed, indicative of a small fraction of meso- and macropores. Hg intrusion porosimetry further confirmed the hierarchical pore structure (Fig. S1b). The intrusion profile was concentrated in the meso- to macropore range (10^2–10^3 nm, according to IUPAC classification [52], while the extrusion curve extended more broadly (10^2–10^4 nm), displaying pronounced hysteresis typical of mercury extrusion processes. The average pore size determined by intrusion was ≈500 nm, confirming that the majority of pores in binder-free 5 A belong to the macropore regime. SEM micrographs (Figs. S1c–f) revealed well-faceted crystals with an average size of ≈2 μm (2×10^3 nm), exhibiting predominantly cubic to near-spherical morphologies, characteristic of LTA-type zeolites.

3.2. Adsorption equilibrium isotherms

Pure-component adsorption equilibrium data for CO_2 and N_2 on binder-free LTA zeolites were obtained from breakthrough experiments at 306, 326, and 344 K and partial pressures of 10, 40, 120, and 350 kPa. The corresponding DSL model fitting parameters are provided in Table S5. It should be noted that the equilibrium measurements were performed at selected pressure points relevant to post-combustion capture conditions to enable consistent comparison across materials and direct integration with dynamic breakthrough modeling, rather than to generate high-density isotherm datasets.

Fig. 1 compares the CO_2 adsorption isotherms for binder-free 4 A, 5 A, Sr(40)A, and Sr(80)A at (Fig. 1a) 306 K, (Fig. 1b) 326 K, and (Fig. 1c) 344 K. Across all conditions, 5 A exhibited the highest capacity, followed by Sr(40)A, Sr(80)A, and 4 A. The enhanced performance of Ca^{2+}-exchanged 5 A reflects the introduction of stronger adsorption sites coupled with enlarged pore apertures [16], which facilitate greater CO_2

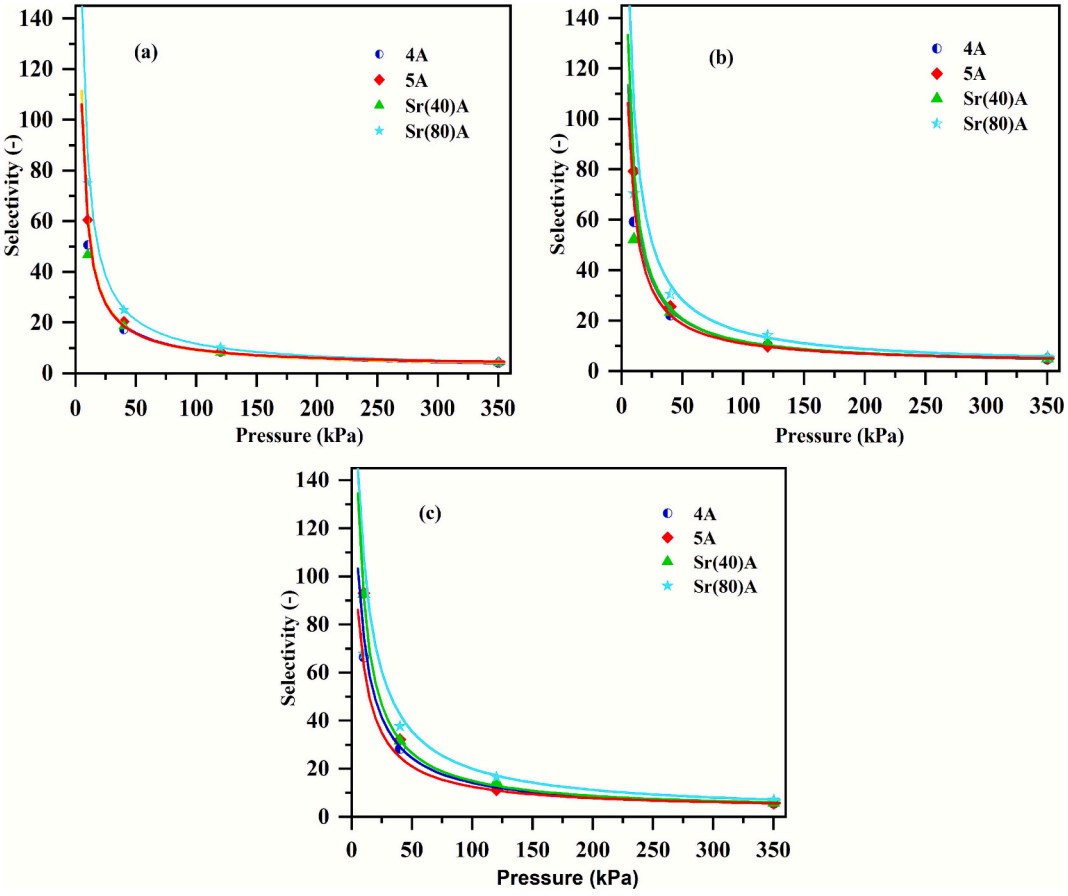

Fig. 3. Selectivity of CO_2/N_2 at **(a)** 306, **(b)** 326, and **(c)** 344 K for binder-free 4 A, 5 A, Sr(40)A, Sr(80)A zeolite. Experimental = symbols; DSL isotherm = lines.

accommodation within the LTA framework. At 120 kPa and 306 K, the CO_2 loading reached 5.58 mol•kg^{-1} for 5 A, compared with 4.47 mol•kg^{-1} for Sr(40)A, 4.45 mol•kg^{-1} for Sr(80)A, and 3.73 mol•kg^{-1} for 4 A. The similarity between Sr(40)A and Sr(80)A confirms that Sr^{2+} incorporation significantly enhances uptake relative to 4 A, but the incremental benefit diminishes beyond a certain exchange degree. These observations highlight the pivotal role of cation identity and distribution in governing CO_2–framework electrostatic interactions and, consequently, adsorption affinity.

The N_2 isotherms (Fig. 2) displayed nearly linear behavior, consistent with the weak quadrupole moment of N_2 and its limited interaction with extra-framework cations. The adsorption hierarchy generally mirrored that of CO_2, with the exception that Sr(80)A exhibited the lowest uptake. At 326 K and 350 kPa, Sr(80)A adsorbed 0.78 mol•kg^{-1} of N_2–2.6% lower than 4 A, 17.0% lower than Sr(40)A, and 31.0% lower than 5 A. Suppressed N_2 adsorption is advantageous for separation, as it enhances CO_2/N_2 selectivity. This behavior suggests that Sr^{2+} exchange not only strengthens CO_2 adsorption sites but also disfavors N_2 uptake, thereby amplifying separation performance under flue gas–relevant conditions.

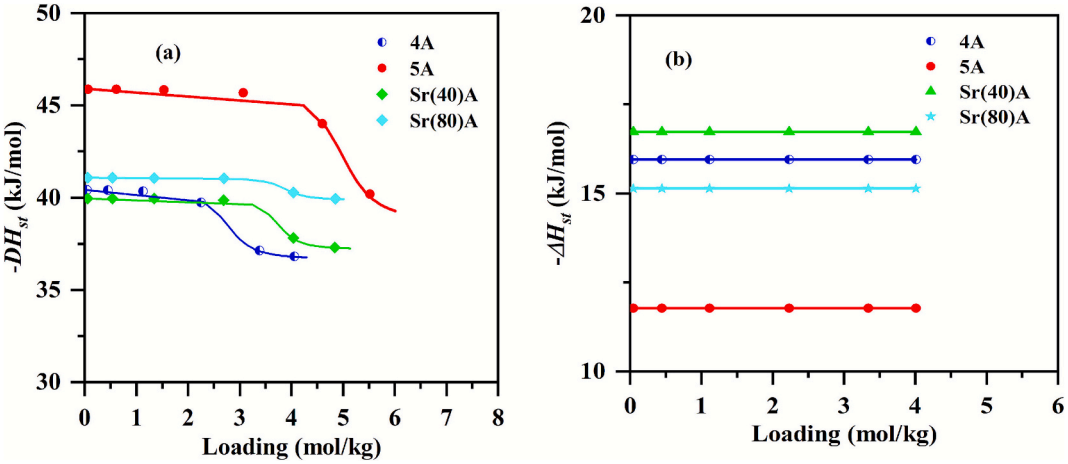

Fig. 4. Isosteric heats of sorption plotted against loading for **(a)** CO_2 and **(b)** N_2. Experimental = symbols; Numerical (Eq. S1, Supporting Information) = lines.

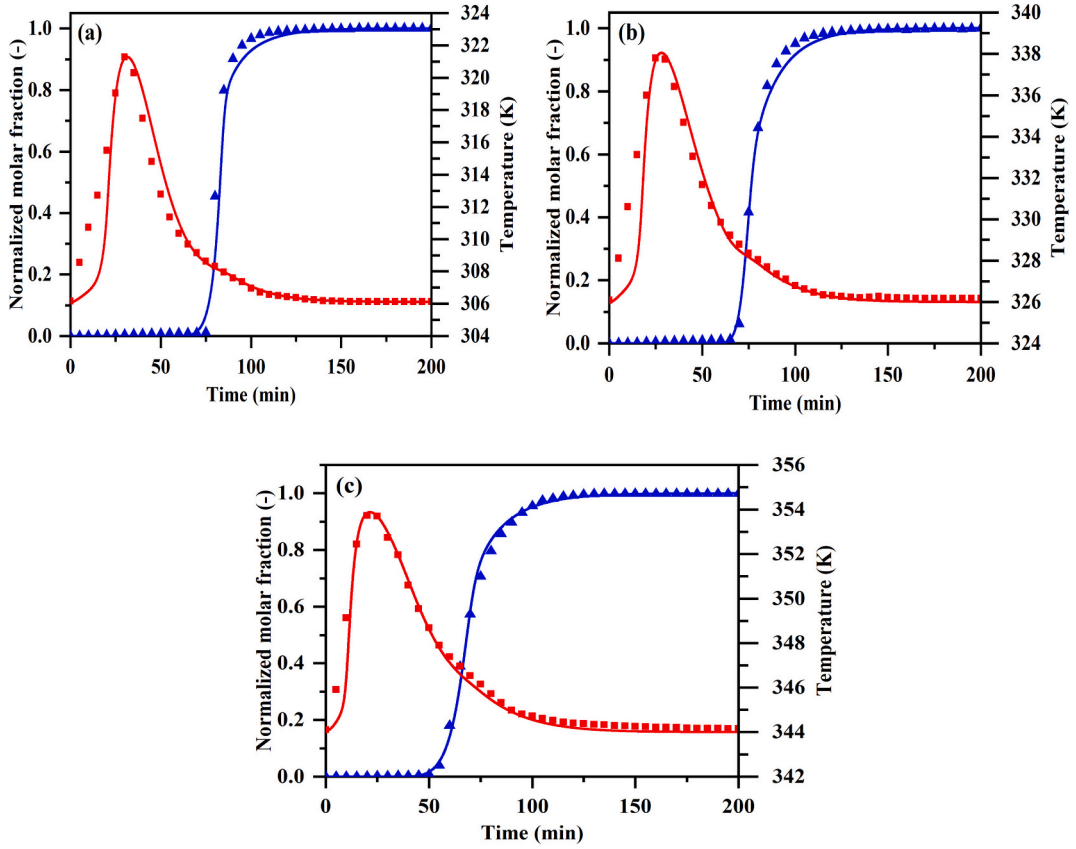

Fig. 5. Breakthrough curves (▲) and temperature fronts at the middle position of the bed (■) for binder-free 5 A zeolite in pure CO_2 fixed bed experiments at **(a)** 306, **(b)** 326, and **(c)** 344 K and 50 kPa partial pressure. Experimental = symbols; Aspen numerical predictions = lines.

3.3. Separation indicators

The CO_2/ N_2 adsorption selectivities of the binder-free LTA zeolites are compared in Fig. 3. Sr(80)A clearly stands out, delivering the highest selectivity of 75 at 10 kPa and 306 K, relative to 60 for 5 A, 51 for 4 A, and 47 for Sr(40)A. Examination of the selectivity profiles across temperatures (Figs. 3a–c) reveals a consistent upward trend with increasing temperature. At 40 kPa and 306 K, the selectivities were 17 (4 A), 20 (5 A), 19 (Sr(40)A), and 25 (Sr(80)A). At 344 K, these values increased by 64.7%, 60.0%, 63.2%, and 52.0%, respectively. This systematic enhancement indicates that N_2 adsorption is more temperature-sensitive than CO_2, thereby amplifying separation performance under elevated-temperature conditions. Overall, these results highlight the strong potential of Sr(80)A as a highly selective adsorbent for post-combustion CO_2 capture. The combination of high intrinsic selectivity and improved performance at higher temperatures makes Sr-exchanged LTA zeolites particularly attractive for integration into industrial flue-gas treatment systems. It should be noted that the enhanced CO_2 adsorption and selectivity observed for divalent-cation-exchanged LTA zeolites are interpreted here based on macroscopic adsorption thermodynamics, breakthrough behavior, and established literature, rather than direct molecular-scale characterization. Future studies employing in situ spectroscopic techniques or molecular simulations would be highly valuable to directly elucidate the nature and strength of CO_2–cation interactions in these systems [32,34–36,53].

The strength and nature of adsorbate–adsorbent interactions were further examined through isosteric heat analysis. Fig. 4 compares the heats of adsorption predicted by the DSL model (Eq. S1, Supporting Information) with those obtained experimentally (Eq. S5) for **(a)** CO_2 and **(b)** N_2 across all binder-free LTA zeolites. The isosteric heats of adsorption were calculated from temperature-dependent DSL fits using the Clausius–Clapeyron relation; therefore, the reported heat values reflect model-based interpolation, and their physical relevance should be considered primarily within the experimentally observed loading range and care must be taken with extrapolated data regarding N_2 above 1.5 mol/kg. As expected, the magnitude of $-\Delta H$ follows the hierarchy $CO_2 \gg N_2$, with values ranging from 45.9 to 36.6 kJ•mol^{-1} for CO_2 and from 16.8 to 12.4 kJ•mol^{-1} for N_2. The degree of energetic heterogeneity is dictated by molecular properties such as size, polarity, and quadrupole moment [54]. CO_2, with its substantial quadrupole moment, strongly interacts with the electrostatic field gradients induced by extra-framework cations, resulting in elevated adsorption energies [55]. In contrast, N_2, being nonpolar and characterized by negligible dipole and quadrupole moments [56,57], engages in much weaker interactions, yielding lower and nearly constant isosteric heat values across the loading range (Fig. 4b). For CO_2, the gradual decline in $-\Delta H$ with increasing uptake (Fig. 4a) indicates preferential filling of high-energy sites followed by progressive occupation of lower-energy sites, confirming the energetic heterogeneity within the LTA cavities. Higher values of $-\Delta H$ correspond to stronger binding forces and enhanced affinity toward CO_2. Among the materials examined, binder-free 5 A demonstrated the highest $-\Delta H$, decreasing from 45.9 to ~39 kJ•mol^{-1}, which aligns with its superior CO_2 capacity and highlights the strong Ca^{2+}–CO_2 electrostatic interactions responsible for its performance.

3.4. CO_2 single-component breakthrough experiments

The dynamic behavior of CO_2 adsorption on binder-free 5 A zeolite was investigated through both experimental and simulated breakthrough curves, as shown in Fig. 5. Experiments were performed at a CO_2 partial pressure of 50 kPa (balanced with He) and temperatures of (Fig. 5a) 306 K, (Fig. 5b) 326 K, and (Fig. 5c) 344 K. The breakthrough

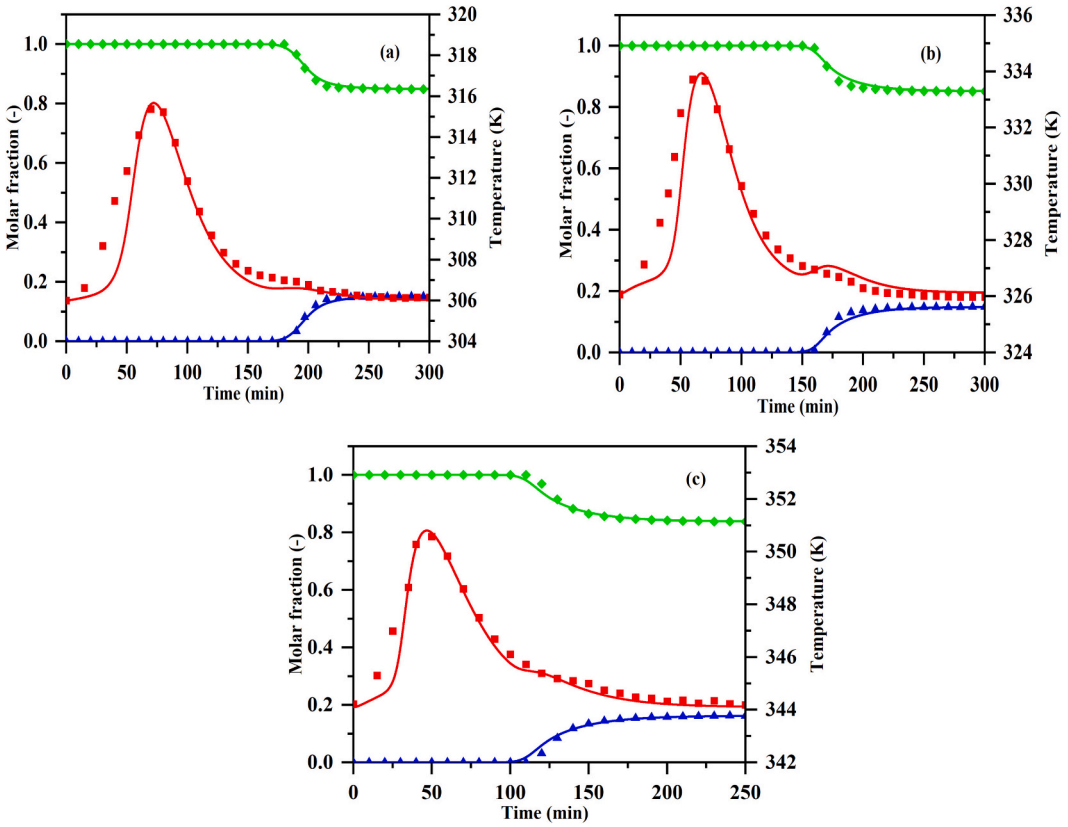

Fig. 6. Breakthrough curves for binder-free 5 A zeolite in binary CO_2 (15%) (▲) and N_2 (85%)(◆) fixed bed experiments and temperature fronts (■) at **(a)** 306, **(b)** 326, and **(c)** 344 K. Experimental = symbols; Aspen numerical predictions = lines.

profiles are expressed as mole fractions normalized to the feed composition, while the corresponding temperature fronts, monitored at the column midpoint, are presented on the right Y-axis. The transport parameters applied in the Aspen Adsorption simulations are listed in Tables S6 (Supporting Information). The results confirm the strong CO_2 affinity of 5 A, with clear temperature dependence. Retention times decreased from ~75 min at 306 K to ~60 min at 326 K and ~ 50 min at 344 K, consistent with exothermic adsorption behavior. Temperature fronts further illustrate this effect, showing maximum rises of 16 K at 306 K (322*K*), 12 K at 326 K (338 K), and 10 K at 344 K (354 K).

A high degree of consistency was observed between experimental data (symbols) and simulated profiles (lines), demonstrating the predictive accuracy of the Aspen Adsorption model. The simulations successfully reproduced both the shape and timing of the breakthrough curves as well as the magnitude of the temperature excursions, thereby validating the reliability of the transport parameters and correlations employed. This strong agreement highlights the capability of the modeling framework to describe adsorption dynamics with high fidelity, supporting its application for process design and scale-up.

3.5. CO_2/N_2 binary breakthrough experiments

The binary adsorption dynamics of CO_2/N_2 on binder-free 5 A zeolite were examined through breakthrough experiments, with results presented in Fig. 6 for three temperatures: 306 K (Fig. 6a), 326 K (Fig. 6b), and 344 K (Fig. 6c). The corresponding transport parameters used in the simulations are provided in Table S7. The breakthrough duration of CO_2 decreased with increasing temperature, from ~175 min at 306 K to ~100 min at 344 K, consistent with the reduction in adsorption capacity at elevated temperatures. Temperature fronts exhibited peak rises to ~316 K, 334 K, and 351 K at 306, 326, and 344 K, respectively, with shorter durations at higher temperatures reflecting accelerated breakthrough behavior. Computational simulations performed in Aspen Adsorption showed excellent agreement with the experimental data, validating the predictive capability of the model for describing CO_2/N_2 separation in the LTA framework. Both the timing of breakthrough and the magnitude of temperature excursions were reproduced with high fidelity, confirming the reliability of the transport correlations applied in this study.

To further probe the role of mass-transfer phenomena, a parametric sensitivity study was conducted using Aspen Adsorption v10. Two sets of simulations were performed: (i) varying axial dispersion while holding the overall mass-transfer coefficient constant, and (ii) varying the mass-transfer coefficient while keeping axial dispersion fixed. As shown in Fig. S3 (Supporting Information), axial dispersion strongly influenced the shape of the concentration profiles, with higher dispersion leading to broader spreading of the breakthrough curves. In contrast, variations in the overall mass-transfer coefficient produced minimal changes in curve profiles. These results demonstrate that zone spreading in the adsorption bed is governed predominantly by axial dispersion, underscoring its critical role in shaping breakthrough behavior in fixed-bed CO_2/N_2 separations.

It is worth noting that the binary breakthrough experiments conducted in this study are intended as controlled benchmark tests to compare the intrinsic separation behavior of ion-exchanged, binder-free LTA zeolites under representative post-combustion conditions. While variations in feed composition, cyclic operation, and humidity are critically important for industrial deployment, they are beyond the scope of the present work. Nevertheless, the validated dynamic model implemented in Aspen Adsorption provides a flexible and scalable framework for extending the present analysis toward more realistic post-combustion capture scenarios. Once calibrated against the experimental breakthrough data, the model can be readily adapted to simulate cyclic adsorption processes (e.g., PSA, VPSA, or TSA) through

Table 1
The results of analysis of variance (ANOVA) of selectivity of 4 A for CO_2/N_2 separation at studied temperatures and pressures.

	Sum of squares	*Mean squares*	*Coded coefficient*	*Standard error*	*Df*	*p-value*
Model	18.51	3.70			5	<0.0001
T	0.97	0.97	0.083	0.006	1	<0.0001
P	14.89	14.89	−0.45	0.008	1	<0.0001
T × P	0.00006	0.00006	−0.0001	0.010	1	0.9914
T^2	0.00007	0.00007	−0.004	0.011	1	0.6994
P^2	2.63	2.63	0.36	0.016	1	<0.0001
Residual	1.10	0.005			207	–
Total	19.61	–			212	–
Std. dev.	0.073					
R^2	0.95					
Adj-R^2	0.95					
Pred-R^2	0.94					
Developed approach:						
$Log_{10}(SelectivityCO_2/N_2) = -0.59 + (0.01 \times T) - (6.84e^{-3} \times P) - (3.084e^{-8} \times T \times P) - (9.33e^{-6} \times T^2) + (1.18e^{-5} \times P^2)$						

Table 2
The results of analysis of variance (ANOVA) of selectivity of 5 A for CO_2/N_2 separation at studied temperatures and pressures.

	Sum of squares	*Mean squares*	*Coded coefficient*	*Standard error*	*Df*	*p-value*
Model	15.41	3.08			5	<0.0001
T	0.40	0.40	0.053	0.006	1	<0.0001
P	12.33	12.33	−0.41	0.008	1	<0.0001
T × P	0.0002	0.0002	−0.002	0.011	1	0.8567
T^2	0.001	0.001	−0.005	0.011	1	0.6321
P^2	2.68	2.68	0.37	0.017	1	<0.0001
Residual	1.18	0.006			207	–
Total	16.59				212	–
Std. dev.	0.075					
R^2	0.93					
Adj-R^2	0.93					
Pred-R^2	0.92					
Developed approach:						
$Log_{10}(SelectivityCO_2/N_2) = -0.48 + (0.01 \times T) - (6.47e^{-3} \times P) - (5.32e^{-7} \times T \times P) - (1.2e^{-5} \times T^2) + (1.2e^{-5} \times P^2)$						

appropriate step sequencing, boundary conditions, and cycle scheduling. Moreover, moisture effects—via competitive adsorption equilibria and transport parameters available in the literature—can be systematically incorporated within the same modeling framework. However to use the data shown through this work in the development of PSA/VPSA cyclic operations guard beds (e.g zeolite 3 A) must be used to capture humidity on the PCC streams As such, the current experimental–modeling integration establishes a robust foundation for future cyclic process simulations aimed at evaluating separation performance, productivity, and energy requirements under industrially relevant post-combustion conditions. However, the same methodology of gas adsorption process design model can be used for humid streams if the corresponding thermodynamic data is available on such conditions.

3.6. Statistical analysis by RSM

Response Surface Methodology (RSM) was systematically applied to all investigated LTA zeolites (4 A, 5 A, Sr(40)A, and Sr(80)A) using the Historical Data module within the RSM framework. For each material, independent statistical correlations were developed to quantify adsorption selectivity under varying operating conditions. Multiple regression analysis, combined with analysis of variance (ANOVA), was employed to evaluate model adequacy, identify statistically significant terms, and assess potential lack-of-fit. The initial polynomial models were rigorously examined using standard statistical metrics, including *p*-values, standard deviation, coefficients of determination (R^2, adjusted R^2, and predicted R^2), and lack-of-fit tests. Insignificant terms and interactions were subsequently eliminated, resulting in reduced models with improved robustness and predictive accuracy.

In this context, RSM was employed to identify temperature–pressure regions corresponding to maximum CO_2/N_2 selectivity, providing guidance for future experimental investigations and cyclic adsorption simulations rather than introducing new fundamental adsorption insights. The ANOVA outcomes for all adsorbents are summarized in Tables 1–4, while the corresponding response surface plots are presented in Fig. 7. All final models exhibit strong statistical significance ($p < 0.0001$) with no meaningful lack-of-fit, confirming their validity (See Tables 1–4). Furthermore, the obtained values of R^2, adjusted R^2, and standard deviation fall within acceptable ranges for reliable prediction. For example, zeolite 4 A shows R^2, adjusted R^2, and predicted R^2 values of 0.95, 0.95, and 0.94, respectively (Table 1). The final regression equations—expressed in terms of real operating variables rather than coded factors—are also provided in Tables 1–4.

Inspection of the coded coefficients reveals that linear terms exert the dominant influence on selectivity. For instance, the linear coefficients associated with temperature and pressure for Sr(80)A (0.11 and − 0.49, respectively; Table 4) indicate that temperature has a positive effect on selectivity, whereas increasing pressure reduces it. This trend is consistent across all materials, as evidenced by the positive temperature coefficients (e.g., 0.97 for 4 A, Table 1) and negative pressure coefficients (e.g., −0.41 for 5 A, Table 2). The interaction terms further suggest that at elevated temperatures, the adverse effect of pressure on selectivity becomes less pronounced. These statistical observations are fully consistent with the experimental trends discussed earlier in Section 3.3.

Analysis of the response surface plots (Fig. 7) indicates that Sr(80)A achieves the highest selectivity, highlighting its strong potential for CO_2/N_2 separation. Building on this insight, an optimization procedure was performed using 30 iterative runs for each model to identify operating conditions that maximize CO_2/N_2 selectivity for Sr(80)A in cyclic

Table 3
The results of analysis of variance (ANOVA) of selectivity of Sr(40)A for CO_2/N_2 separation at studied temperatures and pressures.

	Sum of squares	*Mean squares*	*Coded coefficient*	*Standard error*	*Df*	*p-value*
Model	18.96	3.79			5	<0.0001
T	1.22	1.22	0.093	0.006	1	<0.0001
P	14.72	14.72	−0.44	0.009	1	<0.0001
T × P	0.014	0.014	−0.017	0.011	1	0.1339
T^2	0.00002	0.00002	0.0002	0.012	1	0.9831
P^2	2.98	2.98	0.39	0.018	1	<0.0001
Residual	1.31	0.006			207	–
Total	20.28	–			212	–
Std. dev.	0.081					
R^2	0.94					
Adj-R^2	0.94					
Pred-R^2	0.93					
Developed approach:						
$Log_{10}(SelectivityCO_2/N_2) = +0.06 + (4.89e^{-3} \times T) - (5.57e^{-3} \times P) - (4.68e^{-6} \times T \times P) + (5.58e^{-7} \times T^2) + (1.26e^{-5} \times P^2)$						

Table 4
The results of analysis of variance (ANOVA) of selectivity of Sr(80)A for CO_2/N_2 separation at studied temperatures and pressures.

	Sum of squares	*Mean squares*	*Coded coefficient*	*Standard error*	*Df*	*p-value*
Model	21.81	4.36			5	<0.0001
T	1.57	1.57	0.11	0.006	1	<0.0001
P	17.36	17.36	−0.49	0.008	1	<0.0001
T × P	0.00005	0.00005	−0.001	0.011	1	0.9181
T^2	0.0002	0.0002	−0.002	0.011	1	0.8309
P^2	2.87	2.87	0.38	0.017	1	<0.0001
Residual	1.13	0.005			207	–
Total	22.94	–			212	–
Std. dev.	0.074					
R^2	0.95					
Adj-R^2	0.94					
Pred-R^2	0.94					
Developed approach:						
$Log_{10}(SelectivityCO_2/N_2) = -0.33 + (8.37e^{-3} \times T) - (7.34e^{-3} \times P) + (2.97e^{-7} \times T \times P) - (5.23e^{-6} \times T^2) + (1.23e^{-5} \times P^2)$						

adsorption applications. The RSM-based optimization yielded an optimal selectivity value of 83, corresponding to an operating temperature of 348 K and a pressure of 5 kPa bar, underscoring the applicability of Sr(80)A for advanced separation process design.

3.7. Benchmarking adsorption performance

As already extensively discussed, the binary breakthrough experiments were carried out under standard PCC conditions for all binder-free LTA zeolites. The feed gas mixture contained 15% CO_2 and 85% N_2 (mol %) at 101 kPa and 306 K. The evaluation of CO_2 separation performance followed established methodologies [44,58,59], including assessment of CO_2 loadings, CO_2/N_2 selectivities, and working capacities. A summary of the key metrics alongside other benchmark adsorbents is provided in Table 5. The binary CO_2 loading was 2.78 mol•kg^{-1} for 4 A, 4.81 mol•kg^{-1} for 5 A, 3.68 mol•kg^{-1} for Sr(40)A, and 3.62 mol•kg^{-1} for Sr (80)A. Interestingly, the CO_2/N_2 selectivity followed a slightly different hierarchy, with Sr(80)A achieving the highest value of 65, followed by 5 A (52), Sr(40)A (50), and 4 A (47). These findings are consistent with the equilibrium selectivity profiles shown in Fig. 3. The comparatively weaker performance of binder-free 4 A in both CO_2 loading and selectivity can be attributed to its narrower pore size, reduced accessibility of adsorption sites, and slower diffusion kinetics relative to the Ca^{2+}- and Sr^{2+}-exchanged materials.

Working capacities were further calculated for VPSA-based PCC processes across regeneration pressures of 3, 10, and 15 kPa, relative to a feed pressure of 101 kPa, following prior studies [60–62]. For these evaluations, a CO_2 feed molar fraction of 15% and a regeneration composition of 90% CO_2 were assumed to approximate realistic operating conditions. Within the pressure range of 3–101 kPa, binder-free 5 A delivered the highest CO_2 working capacity of 1.20 mol•kg^{-1}, surpassing 4 A by 28.3%, Sr(40)A by 29.2%, and Sr(80)A by 10.8%. Fig. S2 (Supporting Information) compares the CO_2 working capacities of the LTA zeolites under these regeneration scenarios, highlighting Sr (80)A as the second-best performer. Its strong performance is primarily attributed to its elevated CO_2/N_2 selectivity, which favors CO_2 adsorption and maximizes utilization of the framework's adsorption sites. Taken together, the results confirm that while both 5 A and Sr(80)A exhibit strong performance, 5 A offers the most balanced profile for PCC applications, combining superior CO_2 capacity with high working capacity across realistic VPSA conditions. Sr(80)A, however, demonstrates competitive selectivity and remains a promising alternative for scenarios where maximizing separation efficiency is prioritized. However, while the separation mechanism discussed here is supported by experimental adsorption trends, isosteric heat analysis, and dynamic breakthrough behavior, future molecular simulations (e.g., GCMC or DFT) would be highly valuable to directly probe the adsorption sites and interaction energies governing CO_2/N_2 separation in ion-exchanged LTA zeolites, which some helpful details can be found in [32–36,53,63].

4. Conclusions

Adsorption equilibrium measurements of CO_2 and N_2 on ion-exchanged binder-free LTA zeolites were obtained from fixed-bed breakthrough experiments. At 120 kPa and 306 K, CO_2 capacities followed the order 5 A (5.58 mol•kg^{-1}) > Sr(40)A (4.47 mol•kg^{-1}) ≈ Sr (80)A (4.45 mol•kg^{-1}) > 4 A (3.73 mol•kg^{-1}). The superior uptake of 5 A arises from Ca^{2+} substitution, which enlarges pore apertures and

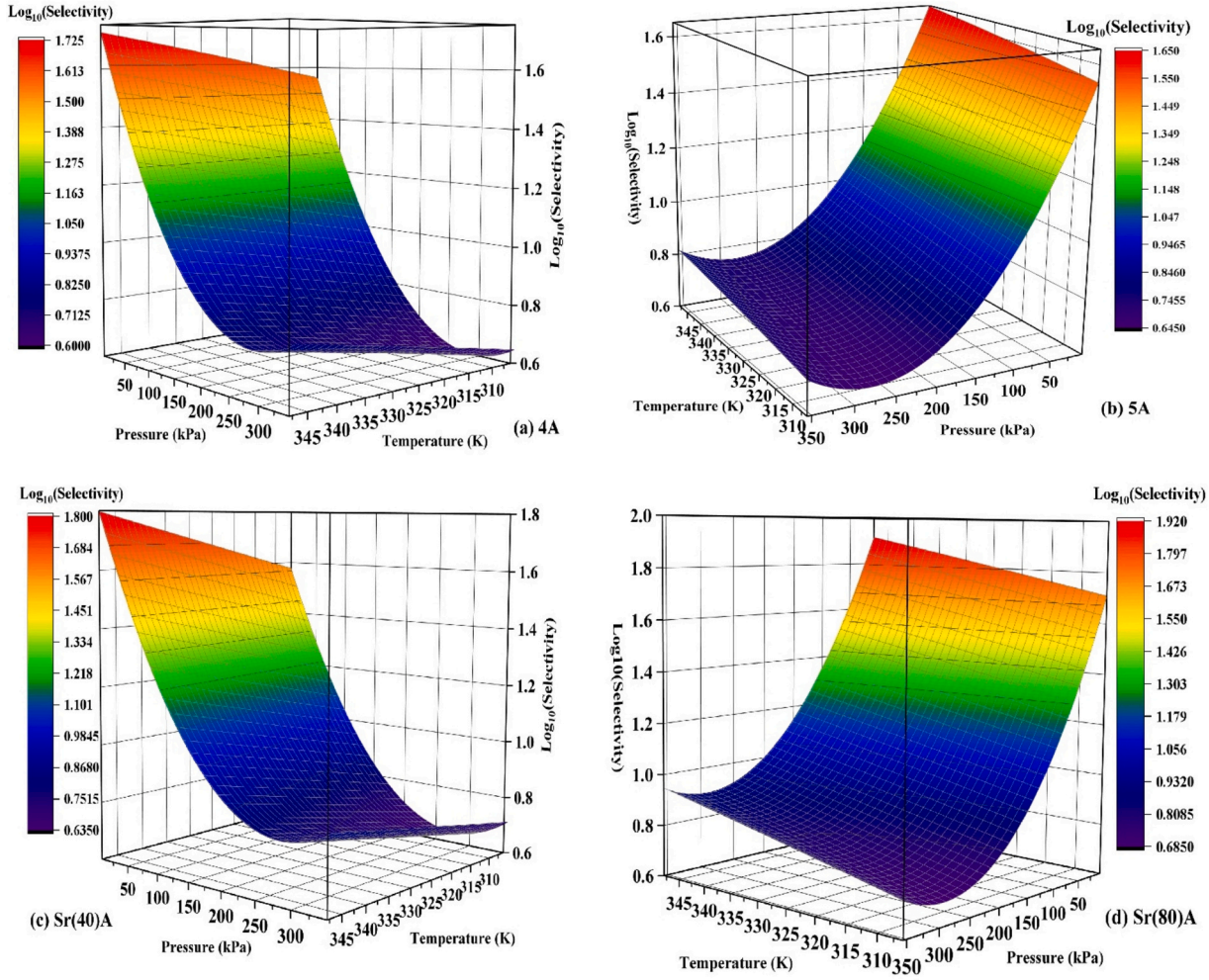

Fig. 7. Response surface plots of selectivity for **(a)** 4 A, **(b)** 5 A, **(c)** Sr(40)A and **(d)** Sr(80)A zeolites for CO_2/N_2 separation, as a function of the independent variables.

Table 5
Comparison of adsorption performance metrics for various LTA zeolites under PCC conditions, alongside other benchmark adsorbents.

	Flue gas conditions: CO_2/N_2 (15/85 Mol%), 306 K, 101 kPa					
Adsorbents	Binary CO_2 loading q_{bCO2} (Mol •kg $^{-1}$)	Binary CO_2/N_2 selectivity $\alpha_{bCO_2/N_2}(-)$	Working capacity β_1 (Mol •kg $^{-1}$)	Working capacity β_2 (Mol •kg $^{-1}$)	Working capacity β_3 (Mol •kg $^{-1}$)	Ref.
Binder-free zeolites						
4A	2.78	46.8	0.860	0.218	0.0441	This study
5A	4.81	51.7	1.20	0.270	0.0522	This study
Sr(40)A	3.68	49.7	0.847	0.194	0.0384	This study
Sr(80)A	3.62	64.5	1.07	0.232	0.0438	This study
NaY	3.29	89	2.01	0.66	0.14	[64]
K(95)Y	4.12	83	2.25	0.63	0.12	[64]
Ca(56)Y	1.98	58	1.26	0.44	0.09	[64]
Ca(71)Y	1.52	52	1.06	0.39	0.09	[64]
Other adsorbents						
Zeolite 13X	3.14	80	1.28	0.41	0.09	[65]
Mg-MOF-74	6.07	52	2.26	0.53	0.10	[66]
UTSA-16	1.64	152	1.65	0.61	0.13	[67]
CS-AS	0.77	17	0.76	0.35	0.08	[68]

Conditions:
$\beta_1$ads: q (T1, P1) = q (306 K, 101 kPa). $\beta_1$des: q (T2, P2) = q (306 K, 3 kPa).
$\beta_2$ads: q (T1, P1) = q (306 K, 101 kPa). $\beta_2$des: q (T2, P2) = q (306 K, 10 kPa).
$\beta_3$ads: q (T1, P1) = q (306 K, 101 kPa). $\beta_3$des: q (T2, P2) = q (306 K, 15 kPa).

enhances accommodation of CO_2 within the framework. Sr-exchanged zeolites also outperformed 4 A, owing to high-energy adsorption sites created by Sr^{2+} ions positioned within the supercages. In contrast, N_2 adsorption displayed a more linear profile, with Sr(80)A showing the lowest uptake (0.78 mol•kg^{-1} at 326 K and 350 kPa). This reduced N_2 uptake translates into higher CO_2/N_2 separation performance. Also, Sr (80)A achieved the highest CO_2/N_2 selectivity (75 at 10 kPa and 306 K), surpassing 5 A (60), 4 A (51), and Sr(40)A (47). Binary adsorption experiments under PCC conditions confirmed these observations: Sr(80)A consistently delivered the highest selectivity, while 5 A exhibited the largest CO_2 working capacity (1.20 mol•kg^{-1} across 3–101 kPa), exceeding 4 A, Sr(40)A, and Sr(80)A by 28.3%, 29.2%, and 10.8%, respectively. Finally, the RSM was employed for statistical analysis of different studied zeolites concerning their performance for CO_2/N_2 separation and getting the optimum operating conditions. Taken together, these findings highlight the strong potential of ion-exchanged binder-free LTA zeolites, particularly Sr(80)A and 5 A, as efficient and scalable adsorbents for CO_2 capture. The insights obtained from these single-cycle, dry binary breakthrough experiments provide a robust basis for material screening and dynamic model validation and can serve as a foundation for future investigations under cyclic in dried and humid post-combustion conditions.

Declaration of competing interest

The authors declare that they have no known competing financial interests or personal relationships that could have appeared to influence the work reported in this paper.

Acknowledgments

This work was supported by national funds through FCT/MCTES (PIDDAC): CIMO UID/00690/2025 (10.54499/UID/00690/2025) and UID/PRR/00690/2025 (10.54499/UID/PRR/00690/2025); SusTEC, LA/P/0007/2020 (DOI: 10.54499/LA/P/0007/2020); and (3) CICECO – Aveiro Institute of Materials, UIDB/50011/2020, UIDP/50011/2020, and LA/P/0006/2020. The authors also gratefully acknowledge Kristin Gleichmann and Chemiewerk Bad Köstritz GmbH, Heinrichshall, Germany for valuable support in providing the binder-free LTA zeolite samples used in this study.

Appendix A. Supplementary data

Supplementary data to this article can be found online at https://doi.org/10.1016/j.seppur.2026.137050.

Data availability

Data will be made available on request.

References

[1] W. Gao, S. Liang, R. Wang, Q. Jiang, Y. Zhang, Q. Zheng, B. Xie, C.Y. Toe, X. Zhu, J. Wang, L. Huang, Y. Gao, Z. Wang, C. Jo, Q. Wang, L. Wang, Y. Liu, B. Louis, J. Scott, A.C. Roger, R. Amal, H. He, S.E. Park, Industrial carbon dioxide capture and utilization: state of the art and future challenges, Chem. Soc. Rev. 49 (2020) 8584–8686, https://doi.org/10.1039/D0CS00025F.

[2] IPCC, Climate Change 2022: Impacts, Adaptation and Vulnerability. Contribution of Working Group II to the Sixth Assessment Report of the Intergovernmental Panel on Climate Change, Cambridge University Press, Cambridge, UK and New York, NY, USA, 2022, p. 3056.

[3] M. Karimi, J.A.C. Silva, C.N.D.P. Gonçalves, J.L. Diaz De Tuesta, A.E. Rodrigues, H. T. Gomes, CO_2 capture in chemically and thermally modified activated carbons using breakthrough measurements: experimental and modeling study, Ind. Eng. Chem. Res. 57 (2018) 11154–11166, https://doi.org/10.1021/ACS.IECR.8B00953.

[4] M.N. Dods, E.J. Kim, J.R. Long, S.C. Weston, Deep CCS: moving beyond 90% carbon dioxide capture, Environ. Sci. Technol. 55 (2021) 8524–8534, https://doi.org/10.1021/acs.est.0c07390.

[5] M. Bui, C.S. Adjiman, A. Bardow, E.J. Anthony, A. Boston, S. Brown, P.S. Fennell, S. Fuss, A. Galindo, L.A. Hackett, J.P. Hallett, H.J. Herzog, G. Jackson, J. Kemper, S. Krevor, G.C. Maitland, M. Matuszewski, I.S. Metcalfe, C. Petit, G. Puxty, J. Reimer, D.M. Reiner, E.S. Rubin, S.A. Scott, N. Shah, B. Smit, J.P.M. Trusler, P. Webley, J. Wilcox, N. Mac Dowell, Carbon capture and storage (CCS): the way forward, Energy Environ. Sci. 11 (2018) 1062–1176, https://doi.org/10.1039/C7EE02342A.

[6] B. Smit, R. Graham, P. Styring, J. Yao, P. Clough, J.S.M. Lee, N. Macdowell, S. Lyth, G. Rochelle, T. Hills, G. Wilson, C. Petit, J. Kemper, R. Cuellar-Franca, G. Dowson, M. Gazzani, P. Fennell, D. Sutter, C. Scholes, A. Azapagic, R. Bell, J. Gibbins, M. Mazzotti, G. Maitland, S. Brandani, R. Ocone, M.T. Mota-Martinez, M. Dunstan, P. Liang, R. Anantharaman, L. Joss, J. Stolaroff, CCS – a technology for the future: general discussion, Faraday Discuss. 192 (2016) 303–335, https://doi.org/10.1039/C6FD90053D.

[7] N. Goyal, Y. Bo Hu, F. Li, B. Yuan, Advances in hydrophobic physiadsorbents for CO_2 capture from humid flue gas and direct air, Sep. Purif. Technol. 362 (2025) 131729, https://doi.org/10.1016/J.SEPPUR.2025.131729.

[8] H. Sharma, A. Dhir, Capture of carbon dioxide using solid carbonaceous and non-carbonaceous adsorbents: a review, Environ. Chem. Lett. 19 (2) (2020) 851–873, https://doi.org/10.1007/S10311-020-01118-2.

[9] M. Karimi, M. Shirzad, J.A.C. Silva, A.E. Rodrigues, Carbon dioxide separation and capture by adsorption: a review, Environ. Chem. Lett. 21 (2023) 2041–2084, https://doi.org/10.1007/S10311-023-01589-Z.

[10] M. Kong, L. Song, H. Liao, S. Zhang, Y. Wang, X. Deng, W. Feng, A review on development of post-combustion CO_2 capture technologies: performance of carbon-based, zeolites and MOFs adsorbents, Fuel 371 (2024) 132103, https://doi.org/10.1016/J.FUEL.2024.132103.

[11] S.A. Ganiyu, Review of zeolitic-based sorbents for CO_2 capture: insights into functional modifications, economic feasibility and machine learning-enhanced strategies, Chem. Eng. J. Adv. (2025) 100818, https://doi.org/10.1016/J.CEJA.2025.100818.

[12] M. Karimi, M. Shirzad, J.A.C. Silva, A.E. Rodrigues, Biomass/biochar carbon materials for CO_2 capture and sequestration by cyclic adsorption processes: a review and prospects for future directions, J. CO_2 Util. 57 (2022) 101890, https://doi.org/10.1016/J.JCOU.2022.101890.

[13] F. Khan, M.S. Arman, D. Sharma, Z. Pei, C. Ma, Zeolite types reported in the literature on CO_2 adsorption capacity: status and gaps, Sep. Purif. Technol. 378 (2025) 134596, https://doi.org/10.1016/J.SEPPUR.2025.134596.

[14] C.G. Fotsop, A. Lieb, F. Scheffler, Investigating the impact of heating rates on hydrothermal conversion of heat-treated kaolin into Linde-type LTA zeolite for water vapor sorption, Mater. Adv. 6 (2025) 8078–8091, https://doi.org/10.1039/D5MA00678C.

[15] E.A.P. Dias, D.G. da Silva, M. da C. Amaral, L. dos S. Pereira, D.C. de Melo, W. L. Vasconcelos, CO_2 adsorption by zeolites: state-of-art, techniques and emerging trends, Microporous Mesoporous Mater. 400 (2026) 113904, https://doi.org/10.1016/J.MICROMESO.2025.113904.

[16] D.W. Breck, W.G. Eversole, R.M. Milton, T.B. Reed, T.L. Thomas, Crystalline zeolites. I. The properties of a new synthetic zeolite, type A, J. Am. Chem. Soc. 78 (1956) 5963–5972, https://doi.org/10.1021/JA01604A001.

[17] Z. Tao, Y. Tian, W. Wu, Z. Liu, W. Fu, C.-W. Kung, J. Shang, Development of zeolite adsorbents for CO_2 separation in achieving carbon neutrality, npj Mater. Sustain. 2 (1) (2024) 1–16, https://doi.org/10.1038/s44296-024-00023-x.

[18] K.F. Loughlin, D.M. Ruthven, The sorption and diffusion of ethane in type a zeolites, Chem. Eng. Sci. 27 (1972) 1401–1408, https://doi.org/10.1016/0009-2509(72)85027-9.

[19] T.B. Reed, D.W. Breck, Crystalline zeolites. II. Crystal structure of synthetic zeolite, type A, J. Am. Chem. Soc. 78 (2002) 5972–5977, https://doi.org/10.1021/JA01604A002.

[20] R.J. Harper, G.R. Stifel, R.B. Anderson, Adsorption of gases on 4A synthetic zeolite, Can. J. Chem. 47 (1969) 4661–4670, https://doi.org/10.1139/V69-770.

[21] D.G. Boer, J. Langerak, P.P. Pescarmona, Zeolites as selective adsorbents for CO_2 separation, ACS Appl. Energy Mater. 6 (2023) 2634–2656, https://doi.org/10.1021/ACSAEM.2C03605/ASSET/IMAGES/LARGE/AE2C03605_0014.JPEG.

[22] B.M. Weckhuysen, J. Yu, Recent advances in zeolite chemistry and catalysis, Chem. Soc. Rev. 44 (2015) 7022–7024, https://doi.org/10.1039/C5CS90100F.

[23] A.H. Whaieb, F.T. Jasim, A.A. Abdulrahman, I.M. Khuder, S.A. Gheni, I.M. R. Fattah, N.T. Karakullukcu, Tailoring zeolites for enhanced post-combustion CO_2 capture: a critical review, Curr. Res. Green Sustainable Chem. 10 (2025) 100451, https://doi.org/10.1016/J.CRGSC.2025.100451.

[24] M. Karimi, A.E. Rodrigues, J.A.C. Silva, Designing a simple volumetric apparatus for measuring gas adsorption equilibria and kinetics of sorption. Application and validation for CO_2, CH_4 and N_2 adsorption in binder-free beads of 4A zeolite, Chem. Eng. J. 425 (2021), https://doi.org/10.1016/J.CEJ.2021.130538.

[25] F. Akhtar, Q. Liu, N. Hedin, L. Bergström, Strong and binder free structured zeolite sorbents with very high CO_2-over-N_2 selectivities and high capacities to adsorb CO_2 rapidly, Energy Environ. Sci. 5 (2012) 7664–7673, https://doi.org/10.1039/C2EE21153J.

[26] K.S. Walton, M.B. Abney, M.D. LeVan, CO_2 adsorption in Y and X zeolites modified by alkali metal cation exchange, Microporous Mesoporous Mater. 91 (2006) 78–84, https://doi.org/10.1016/J.MICROMESO.2005.11.023.

[27] D. Saha, Z. Bao, F. Jia, S. Deng, Adsorption of CO_2, CH_4, N_2O, and N_2 on MOF-5, MOF-177, and zeolite 5A, Environ. Sci. Technol. 44 (2010) 1820–1826, https://doi.org/10.1021/ES9032309.

[28] S. Kumar, R. Srivastava, J. Koh, Utilization of zeolites as CO_2 capturing agents: advances and future perspectives, J. CO_2 Util. 41 (2020) 101251, https://doi.org/10.1016/J.JCOU.2020.101251.

[29] Y. Wang, Measurements and modeling of water adsorption isotherms of zeolite Linde-type a crystals, Ind. Eng. Chem. Res. 59 (2020) 8304–8314, https://doi.org/10.1021/ACS.IECR.9B06891.

[30] B. Coughlan, R.G. Shaw, Ion-exchanged zeolite a: Sorptive properties of carbon dioxide and Ammonia, Royal Irish Academy, 1976, https://doi.org/10.1016/j.jcis.2004.06.038.

[31] J.J. Pluth, J.V. Smith, Crystal structure of dehydrated strontium-exchanged zeolite a. absence of near-zero-coordinate strontium(2+) ion. Presence of aluminum complex, J. Am. Chem. Soc. 104 (1982) 6977–6982, https://doi.org/10.1021/JA00389A015.

[32] E. Jaramillo, M. Chandross, Adsorption of small molecules in LTA Zeolites. 1. NH_3, CO_2, and H_2O in zeolite 4A, J. Phys. Chem. B 108 (2004) 20155–20159, https://doi.org/10.1021/JP048078F.

[33] E.J. García, J. Pérez-Pellitero, G.D. Pirngruber, C. Jallut, M. Palomino, F. Rey, S. Valencia, Tuning the adsorption properties of Zeolites as adsorbents for CO_2 separation: best compromise between the working capacity and selectivity, Ind. Eng. Chem. Res. 53 (2014) 9860–9874, https://doi.org/10.1021/IE500207S.

[34] D.A. Faux, Molecular dynamics studies of hydrated zeolite 4A, J. Phys. Chem. B 103 (1999) 7803–7808, https://doi.org/10.1021/JP9907600.

[35] L. Bénariac-Doumal, I. Deroche, H. Nouali, J.L. Paillaud, T. Ors, A.N. Fitch, C. Dejoie, A comparative study of CO2 adsorption in a series of zeolites, Phys. Chem. Chem. Phys. 27 (2025) 10621–10634, https://doi.org/10.1039/D5CP00538H.

[36] C. Chen, W.S. Ahn, CO_2 adsorption on LTA zeolites: effect of mesoporosity, Appl. Surf. Sci. 311 (2014) 107–109, https://doi.org/10.1016/J.APSUSC.2014.04.218.

[37] M. Karimi, L.F.A.S. Zafanelli, J.P.P. Almeida, G.R. Ströher, A.E. Rodrigues, J.A. C. Silva, Novel insights into activated carbon derived from municipal solid waste for CO_2 uptake: synthesis, adsorption isotherms and scale-up, J. Environ. Chem. Eng. 8 (2020) 104069, https://doi.org/10.1016/J.JECE.2020.104069.

[38] D.M. Ruthven, Fundamentals of adsorption equilibrium and kinetics in microporous solids, Mol. Sieves Sci. Technol. 7 (2006) 1–43, https://doi.org/10.1007/3829_007.

[39] D. Do, Adsorption Analysis: Equilibria and Kinetics (with CD Containing Computer Matlab Programs), 1st ed., Imperial College Press, London, 1998.

[40] M. Karimi, A. Ferreira, A.E. Rodrigues, F. Nouar, C. Serre, J.A.C. Silva, MIL-160(Al) as a candidate for biogas upgrading and CO2 capture by adsorption processes, Ind. Eng. Chem. Res. 62 (2023) 5216–5229, https://doi.org/10.1021/ACS.IECR.2C04150/SUPPL_FILE/IE2C04150_SI_001.PDF.

[41] M. Karimi, R.M. Siqueira, A.E. Rodrigues, F. Nouar, J.A.C. Silva, C. Serre, A.F. P. Ferreira, Separation of CO_2/N_2 onto shaped MOF MIL-160(Al) using the pressure swing adsorption process for post-combustion application, Ind. Eng. Chem. Res. 63 (2024) 8785, https://doi.org/10.1021/ACS.IECR.4C00611/ASSET/IMAGES/LARGE/IE4C00611_0010.JPEG.

[42] D.M. Ruthven, Principles of Adsorption and Adsorption Processes, 1st ed., Wiley, New York, 1984.

[43] M. Karimi, R.M. Siqueira, A.E. Rodrigues, F. Nouar, J.A.C. Silva, C. Serre, A. Ferreira, Biogas upgrading using shaped MOF MIL-160(Al) by pressure swing adsorption process: experimental and dynamic modelling assessment, Sep. Purif. Technol. 344 (2024) 127260, https://doi.org/10.1016/J.SEPPUR.2024.127260.

[44] R.T. Yang, Gas Separation by Adsorption Processes, 1st ed., Elsevier, New York, 1987.

[45] F.A. Da Silva, J.A. Silva, A.E. Rodrigues, General package for the simulation of cyclic adsorption processes, Adsorption 5 (1999) 229–244, https://doi.org/10.1023/A:1008974908427/METRICS.

[46] M. Karimi, R.M. Siqueira, M. Shirzad, A.F.P. Ferreira, A.E. Rodrigues, J.A.C. Silva, Integrated experimental, process simulation, and techno-economic assessment of biogas upgrading via pressure/vacuum swing adsorption, Sep. Purif. Technol. 386 (2026) 136571, https://doi.org/10.1016/J.SEPPUR.2025.136571.

[47] R.H. Myers, D.C. Montgomery, C.M. Anderson-Cook, Response Surface Methodology : Process and Product Optimization Using Designed Experiments, 4th ed., Wiley, New York, 2016.

[48] T.F. Gül, M.E. Gönlügür, E. Güler, A. Cihanoğlu, N. Kabay, Effect of asymmetric feed flow rate and temperature on reverse electrodialysis: a response surface methodology approach, Sep. Purif. Technol. 378 (2025) 134671, https://doi.org/10.1016/J.SEPPUR.2025.134671.

[49] M. Karimi, J.L. Diaz de Tuesta, C.N. Carmem, H.T. Gomes, A.E. Rodrigues, J.A. C. Silva, Compost from municipal solid wastes as a source of biochar for CO_2 capture, Chem. Eng. Technol. 43 (2020) 1336–1349, https://doi.org/10.1002/CEAT.201900108.

[50] Z. Guerra-Que, K.S. López-Margalli, J.M. Urrieta-Saltijeral, A.A. Silahua-Pavón, H. Martínez-García, P. García-Alamilla, G.E. Córdova-Pérez, J.C. Arévalo-Pérez, J. G. Torres-Torres, Activated carbon synthesised from lignocellulosic cocoa pod husk via alkaline and acid treatment for methylene blue adsorption: optimisation by response surface methodology, kinetics, and isotherm modelling, RSC Adv. 15 (2025) 47231–47254, https://doi.org/10.1039/D5RA05557A.

[51] C. Nwaoha, B. Liu, P. Tontiwachwuthikul, A. Benamor, CO_2 capture: experiment and prediction of density and viscosity of AMP–DETA blend using artificial neural network (ANN), response surface methodology (RSM), and novel modified-nonlinear model, Sep. Purif. Technol. 382 (2026) 136080, https://doi.org/10.1016/J.SEPPUR.2025.136080.

[52] M. Thommes, K. Kaneko, A.V. Neimark, J.P. Olivier, F. Rodriguez-Reinoso, J. Rouquerol, K.S.W. Sing, Physisorption of gases, with special reference to the evaluation of surface area and pore size distribution (IUPAC technical report), Pure Appl. Chem. 87 (2015) 1051–1069, https://doi.org/10.1515/PAC-2014-1117/MACHINEREADABLECITATION/RIS.

[53] A.A. Elhussien, I. Abdulazeez, H. Alasiri, W.A. Fouad, Exploring zeolite potential for hydrofluorocarbon capture and recycling: insights from molecular simulations, Microporous Mesoporous Mater. 384 (2025) 113442, https://doi.org/10.1016/J.MICROMESO.2024.113442.

[54] R.T. Yang, Adsorbents: Fundamentals and Applications, John Wiley and Sons Inc, 2003, https://doi.org/10.1002/047144409X.

[55] F. Brandani, D.M. Ruthven, The effect of water on the adsorption of CO_2 and C_3H_8 on type X Zeolites, Ind. Eng. Chem. Res. 43 (2004) 8339–8344, https://doi.org/10.1021/IE0401830.

[56] A.D. Buckingham, Molecular quadrupole moments, Q. Rev. Chem. Soc. 13 (1959) 183–214, https://doi.org/10.1039/QR9591300183.

[57] A.D. Buckingham, D.A. Dunmur, R.L. Disch, Quadrupole moments of some simple molecules, J. Am. Chem. Soc. 90 (2002) 3104–3107, https://doi.org/10.1021/JA01014A023.

[58] P.J.E. Harlick, F.H. Tezel, An experimental adsorbent screening study for CO_2 removal from N_2, Microporous Mesoporous Mater. 76 (2004) 71–79, https://doi.org/10.1016/J.MICROMESO.2004.07.035.

[59] A.K. Rajagopalan, A.M. Avila, A. Rajendran, Do adsorbent screening metrics predict process performance? A process optimisation based study for post-combustion capture of CO_2, Int. J. Greenh. Gas Con. 46 (2016) 76–85, https://doi.org/10.1016/J.IJGGC.2015.12.033.

[60] Z. Liu, L. Wang, X. Kong, P. Li, J. Yu, A.E. Rodrigues, Onsite CO_2 capture from flue gas by an adsorption process in a coal-fired power plant, Ind. Eng. Chem. Res. 51 (2012) 7355–7363, https://doi.org/10.1021/IE3005308.

[61] J. Zhang, P.A. Webley, Cycle development and design for CO_2 capture from flue gas by vacuum swing adsorption, Environ. Sci. Technol. 42 (2007) 563–569, https://doi.org/10.1021/ES0706854.

[62] G. Li, P. Xiao, P. Webley, J. Zhang, R. Singh, M. Marshall, G. Li, P. Xiao, P. Webley, J. Zhang, R. Singh, M. Marshall, Capture of CO_2 from high humidity flue gas by vacuum swing adsorption with zeolite 13X, Adsorption 14 (2008) 415–422, https://doi.org/10.1007/S10450-007-9100-Y.

[63] J.M. Castillo, J. Silvestre-Albero, F. Rodriguez-Reinoso, T.J.H. Vlugt, S. Calero, Water adsorption in hydrophilic zeolites: experiment and simulation, Phys. Chem. Chem. Phys. 15 (2013) 17374–17382, https://doi.org/10.1039/C3CP52910J.

[64] E. Aly, L.F.A.S. Zafanelli, A. Henrique, K. Gleichmann, A.E. Rodrigues, F.A. Da Silva Freitas, J.A.C. Silva, Separation of CO_2/N_2 in ion-exchange binder-free beads of zeolite NaY for post-combustion CO_2 capture, Sep. Purif. Technol. 348 (2024) 127722, https://doi.org/10.1016/J.SEPPUR.2024.127722.

[65] R. Haghpanah, R. Nilam, A. Rajendran, S. Farooq, I.A. Karimi, Cycle synthesis and optimization of a VSA process for postcombustion CO_2 capture, AICHE J. 59 (2013) 4735–4748, https://doi.org/10.1002/AIC.14192.

[66] S. Xiang, Y. He, Z. Zhang, H. Wu, W. Zhou, R. Krishna, B. Chen, Microporous metal-organic framework with potential for carbon dioxide capture at ambient conditions, Nat. Commun. 3 (1) (2012) 1–9, https://doi.org/10.1038/ncomms1956.

[67] A. Masala, J.G. Vitillo, G. Mondino, C.A. Grande, R. Blom, M. Manzoli, M. Marshall, S. Bordiga, CO_2 capture in dry and wet conditions in UTSA-16 metal–organic framework, ACS Appl. Mater. Interfaces 9 (2016) 455–463, https://doi.org/10.1021/ACSAMI.6B13216.

[68] D. Xu, J. Zhang, G. Li, P. Xiao, P. Webley, Y.C. Zhai, Effect of water vapor from power station flue gas on CO_2 capture by vacuum swing adsorption with activated carbon, J. Fuel Chem. Technol. 39 (2011) 169–174, https://doi.org/10.1016/S1872-5813(11)60016-9.